

# Core-shell nano rods for efficient photoelectrochemical hydrogen production

Z. G. Yu<sup>1</sup>, C. E. Pryor<sup>2</sup>, W. H. Lau<sup>3</sup>, M. A. Berding<sup>1</sup>, D. B. MacQueen<sup>1</sup>

<sup>1</sup>*SRI International, 333 Ravenswood Avenue,*

*Menlo Park, California 94025, USA*

<sup>2</sup>*Optical Science and Technology Center and Department of Physics and Astronomy,*

*University of Iowa, Iowa City, Iowa 52242, USA and*

<sup>3</sup>*Center for Spintronics and Quantum Computation and Department of Physics,*

*University of California, Santa Barbara, California 93106, USA*

(Dated: October 13, 2005)

## Abstract

We propose core-shell InP-CdS and InP-ZnTe nano rods as photoelectrodes in the efficient photoelectrochemical hydrogen production. Based on our systematic study using strain-dependent  $k.p$  theory, we find that in these heterostructures both energies and wave-function distributions of electrons and holes can be favorably tailored to a considerable extent by exploiting the interplay between quantum confinement and strain. Consequently, these core-shell nano rods with proper dimensions (height, core radius, and shell thickness) can simultaneously satisfy all criteria for effective photoelectrodes in solar-based hydrogen production.

PACS numbers:

## I. INTRODUCTION

Splitting water using a photoelectrochemical (PEC) process for efficient hydrogen production is a promising approach that can ultimately solve the energy problem facing humanity [1]. In the PEC process a semiconductor material absorbs light, resulting in the generation of electron-hole pairs, and thus serves as a photoelectrode. These electrons and holes, instead of running through a circuit, as in photovoltaics, are consumed at the semiconductor-electrolyte interface to effect the splitting of water into hydrogen and oxygen. After several decades' effort, however, the solar-to-hydrogen efficiency remains too low for PEC hydrogen production to be cost-effective for large-scale applications [2]. The major obstacle is to find a suitable semiconductor material to serve as a photoelectrode that simultaneously satisfies four stringent requirements: 1) The semiconductor material must have a band gap in the range of 1.5 – 2.0 eV to capture most of the photons in the solar spectrum; 2) The conduction and valence band edges, or the lowest unoccupied molecular orbital (LUMO) and highest occupied molecular orbital (HOMO), of the materials must overlap the  $\text{H}_2/\text{H}_2\text{O}$  and  $\text{O}_2/\text{H}_2\text{O}$  redox potentials to provide the free energy needed under  $\text{H}_2/\text{O}_2$  evolution conditions; 3) Charge transfer across the semiconductor-liquid interface must be fast compared to the electron-hole recombination; and 4) The semiconductor surface must be chemically stable in the aqueous medium [3]. For a bulk material, the band edges and their relative positions with respect to  $\text{H}_2\text{O}$  redox potentials are intrinsic material properties and can be modified externally only to a limited extent [4]. Hence, considerable efforts in the field of PEC hydrogen production have been devoted to searching for a material that fortuitously meets these four criteria. To date, semiconductor photoelectrodes with a demonstrated high efficiency in splitting water have large band gaps and only make use of the ultraviolet portion of the solar spectrum [5]. On the other hand, semiconductors with smaller band gaps that better match the solar spectral distribution either corrode or become inert in the aqueous media [5]. One of the best photoelectrodes identified for hydrogen production to date is *p*-type  $\text{GaInP}_2$ , which has a band gap of 1.8-1.9 eV [6]. However, its band edges are too negative to effect photoelectrolysis, and more seriously, the material is unstable and susceptible to corrosion in water [7, 8].

The advent of nanotechnology opens new avenues to discovering and synthesizing improved semiconductor photoelectrodes for hydrogen production. Nanostructures have been

frequently used to obtain large surface-to-volume ratios [9], and ultrafine nanoparticles have been explored to modify the local electron polarization and spatially separate photogenerated electrons and holes [10]. However, the most fundamental and fascinating aspect of nanostructures, quantum confinement, has not yet been seriously utilized in PEC hydrogen production. Since all the aforementioned criteria are essentially controlled by the underlying electronic structure of the material, exploiting quantum confinement will in principle enable one to tailor a nanostructure to meet these criteria. We note, however, that simply reducing the size of a single material to the nanometer scale, which in general increases the band gap, is usually not helpful in hydrogen production. This is because for the photoelectrodes stable in water the gap is already too large, whereas for semiconductors with smaller band gaps the quantum confinement does not address the problem of reactivity in water. Here we suggest that nano heterostructures are the places where one can best exploit quantum confinement and strain to effectively tailor the electronic structures for hydrogen production while simultaneously addressing the stability in water.

In this paper, we study core-shell nano rods and examine their electronic structures and wave functions against all the criteria for an effective photoelectrode in PEC hydrogen production. Core-shell nano spheres, while intensively studied, are unsuitable for PEC hydrogen production (as will be shown in the next section). Having scrutinized many nanostructures made of various semiconductors, we find that InP-CdS and InP-ZnTe core-shell nano rods can be tailored to satisfy all these criteria, and therefore are promising nano photoelectrodes. In Sec. II of this paper, we describe our design of core-shell nano rods for hydrogen production. In Sec. III we present our theoretical approach. Section IV is devoted to discussions of results on core-shell InP-CdS and InP-ZnTe nano rods. Finally we summarize our conclusions in Sec. V.

## II. CORE-SHELL NANO RODS FOR HYDROGEN PRODUCTION

To identify materials and structures as efficient photoelectrodes for hydrogen production, we begin with a common semiconductor with a band gap close to the desired value, for example, InP (1.4 eV). To protect it from corrosion in the aqueous environment, we can coat it with a shell to form a core-shell heterostructure. The shell must be stable in water and have a large band gap so that most photons in the solar spectrum can penetrate into the

core for absorption and creation of electron-hole pairs. Once an electron-hole pair is created in the core, it should have a sufficiently long lifetime to complete the redox reactions before the electron and the hole recombine. The most effective way to reduce such a recombination is to spatially separate the electron and the hole immediately upon creation, which can be achieved in a heterostructure with so-called type-II band alignment. In a system with type-II band alignment the conduction and valence band edges of the smaller band gap material are not within the gap of the larger band gap material. In the core-shell structures considered here, where the core has a smaller gap than the shell, type-II band alignment occurs if either the conduction band edge in the shell is lower than that in the core, or the valence band edge in the shell is higher than that in the core. In the former situation, the electron (LUMO) tends to stay in the shell to lower its energy while the hole (HOMO) remain in the core, whereas in the latter the LUMO is distributed in the core while the HOMO is in the shell.

We emphasize that a very strong type-II band alignment (i.e., a large discontinuity in either the conduction or valence band edge) is not beneficial for hydrogen production, because it will necessitate a much larger band gap in the core than required to facilitate the redox reactions, thereby reducing the solar-to-hydrogen efficiency. Thus it is desirable that the core-shell structure have a weak type-II band alignment with either the conduction-band edge or the valence-band edge being similar across the system, which not only retains a high solar-to-hydrogen efficiency, but also provides strong quantum confinement effects in tailoring the electronic structures.

Since the HOMO and LUMO of a system often do not overlap the water redox potentials, it is necessary that the HOMO and LUMO can be tuned either upward or downward. Simply reducing the system size is not an economical approach to improve the overlap since it pushes the HOMO and LUMO to opposite directions, which significantly increases the gap, and consequently the solar-to-hydrogen efficiency would be reduced. A more efficient way is to shift the HOMO and LUMO in the same direction or independently, which can be achieved in a structure where the HOMO and LUMO are spatially separated, as will be shown below.

Finally, to maintain a fast hydrogen and oxygen production, both electrons and holes must transfer from the photoelectrode into the solution quickly and therefore both the core and the shell must be accessible from the solution. This requirement renders spherical core-shell structures, which have been extensively studied both theoretically and experimentally [11–13], unsuitable for PEC hydrogen production, although they are useful in many other

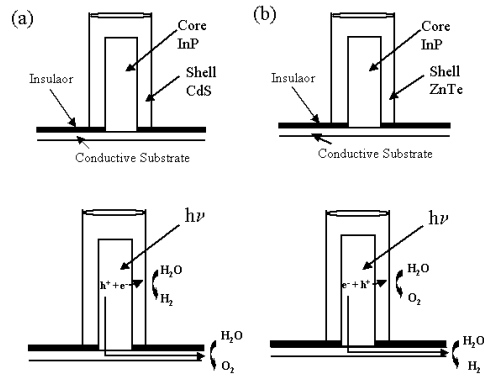


FIG. 1: Schematic device structures showing the core-shell InP-CdS (a) and InP-ZnTe (b) nano rods used in hydrogen production. First, InP rods are grown on a conductive substrate to form cores, then an insulator layer is deposited on the substrate. Finally, CdS or ZnTe are grown to cover the InP cores and form the core-shell nano rods.

applications. Having taken into consideration all these aspects, we identify the core-shell InP-CdS and InP-ZnTe nano rods as efficient photoelectrodes in hydrogen production. In the InP-CdS nano rods, the conduction band edges in the core and in the shell are similar. In the InP-ZnTe nano rods, the valence band edges in different regions are similar.

The envisioned device structures based on the core-shell InP-CdS and InP-ZnTe nano rods for hydrogen production are illustrated in Fig. 1. The shell in such a structure can serve as the anode (cathode) in the electrochemical process of hydrogen production if the hole (electron) is localized in the shell, at whose surface oxygen (hydrogen) is generated. The core is connected to the cathode (anode) through a conductive substrate, on which the structure is grown, to facilitate hydrogen (oxygen) generation. To minimize the interference between electron and hole charge transfer processes, an insulator layer is grown between the shell material and the conductive substrate. For the InP-CdS structure in Fig. 1a, electrons are localized in the shell and holes in the core, whereas for the InP-ZnTe structure in Fig. 1b, electrons are in the core and holes in the shell.

Recent advances in synthesis of nanoparticles and nanostructures give promise of successful fabrication of the proposed device structures in Fig. 1. In particular, high-quality InP nanocrystals with different shapes and dimensions have been synthesized by colloidal chem-

istry methods [24], and further coated by a variety of II-VI materials including CdS, ZnSe, and CdSe with controlled thickness to form core-shell spheres [25]. Possible unpassivated dangling bonds on the surface of the nano rods, which may give rise to undesirable localized states that trap photogenerated electrons and holes, can adversely affect the performance of these photoelectrodes. However, it has been demonstrated that such unpassivated dangling bonds can be effectively eliminated by etching processes [24].

### III. THEORETICAL APPROACH

Due to the lattice mismatch between the materials comprising a core-shell nano rod, the calculation of electronic properties requires a method that accounts for the strain-induced modification of the semiconductor band structure. Nano rod calculations are done numerically, using a well-established technique that has been used for the study of self-assembled strained quantum dots [14]. First, the strain is calculated using linear continuum elastic theory [15] and the finite element method. The calculated strain is then used as input to a real-space strain-dependent  $k.p$  Hamiltonian, using four bands for the valence states and a single-band effective mass model for the conduction states.

The strain distribution in a structure with lattice mismatched materials is obtained by minimizing the elastic energy, given by

$$\begin{aligned}
F = & \int d^3x \frac{1}{2} C_{xxxx} (\sigma_{xx}^2 + \sigma_{yy}^2 + \sigma_{zz}^2) \\
& + C_{xxyy} (\sigma_{xx}\sigma_{yy} + \sigma_{xx}\sigma_{zz} + \sigma_{yy}\sigma_{zz}) \\
& + 2C_{xyxy} (\sigma_{xy}^2 + \sigma_{xz}^2 + \sigma_{yz}^2) - \alpha (\sigma_{xx} + \sigma_{yy} + \sigma_{zz})
\end{aligned} \tag{1}$$

where  $\sigma_{ij}$  is the strain tensor, the  $C$ 's are material-dependent elastic constants, and  $\alpha$  is a parameter used to enforce the lattice mismatch between the two materials. The strain is given in terms of the displacement by  $\sigma_{ij} = \frac{1}{2}(\partial_i u_j + \partial_j u_i)$ .  $F$  is constructed as a function of the  $u$ 's on a cubic grid with derivatives replaced by differences, and then minimized using the conjugate gradient algorithm.

Because the materials to be studied in this paper lack inversion symmetry, the strain produces a polarization given by  $P_i = e_{ijk}\sigma_{jk}$ , leading to an additional electrostatic potential. For zinc-blende semiconductors, the only nonzero elements of the piezoelectric tensor are  $e_{xyz} = e_{zyx} = e_{yzx} \equiv e_{14}$ . From the polarization we can compute the electrostatic potential

$V_p$  by numerically solving the Poisson equation.

The electronic states are computed by Lanczos diagonalization of a real-space representation of the  $k.p$  Hamiltonian on a cubic grid. For the conduction-band states, the Hamiltonian is [16],

$$H_c = E_c - \frac{\hbar^2}{2m_c}(\partial_x^2 + \partial_y^2 + \partial_z^2) + a_c(\sigma_{xx} + \sigma_{yy} + \sigma_{zz}) - eV_p, \quad (2)$$

where  $E_c$  is the conduction band edge of the unstrained system,  $a_c$  is the conduction band hydrostatic deformation potential, and  $m_c$  is the effective mass of conduction-band electrons. To determine the valence-band states, we diagonalize the four-band strain-dependent Hamiltonian [16]

$$H_v = H_v^k + H_v^s - eV_p \quad (3)$$

where

$$H_v^k = - \begin{pmatrix} P - Q & S^* & -R & 0 \\ S & P + Q & 0 & -R \\ -R^* & 0 & P + Q & -S^* \\ 0 & -R^* & -S & P - Q \end{pmatrix}, \quad (4)$$

$$H_v^s = - \begin{pmatrix} p - q + u & s^* + v^* & -r - w & 0 \\ s + v & p + q + u & 0 & -r - w \\ -r^* - w^* & 0 & p + q + u & -s^* - v^* \\ 0 & -r^* - w^* & -s - v & p - q + u \end{pmatrix}, \quad (5)$$

$$\begin{aligned}
P &= -E_v - \gamma_1^L \frac{\hbar}{2m_0} (\partial_x^2 + \partial_y^2 + \partial_z^2), \\
Q &= \gamma_2^L \frac{\hbar}{2m_0} (2\partial_z^2 - \partial_x^2 - \partial_y^2), \\
R &= \frac{\sqrt{3}\hbar}{2m_0} [\gamma_2^L (\partial_x^2 - \partial_y^2) - 2i\gamma_3^L \partial_x \partial_y], \\
S &= -\sqrt{3}\gamma_3^L \frac{\hbar}{m_0} \partial_z (\partial_x - i\partial_y), \\
p &= a_v (\sigma_{xx} + \sigma_{yy} + \sigma_{zz}), \\
q &= b [\sigma_{zz} - \frac{1}{2} (\sigma_{xx} + \sigma_{yy})], \\
r &= \frac{\sqrt{3}}{2} b (\sigma_{xx} - \sigma_{yy}) - id\sigma_{xy}, \\
s &= -d (\sigma_{xz} - i\sigma_{yz}), \\
u &= -\frac{\Delta}{3} (\sigma_{xx} + \sigma_{yy} + \sigma_{zz}), \\
v &= -\frac{2\Delta}{3\sqrt{3}} (\sigma_{xz} - i\sigma_{yz}), \\
w &= -i \frac{2\Delta}{3\sqrt{3}} \sigma_{xy}. \tag{6}
\end{aligned}$$

Here  $E_v$  is the valence band edge of the unstrained system,  $\gamma_i^L$  ( $i = 1, 2, 3$ ) are the Luttinger parameters,  $m_0$  is the free electron mass,  $a_v$  is the valence band hydrostatic deformation potential,  $\Delta$  is the spin-orbit coupling, and  $b$  and  $d$  are shear deformation potentials. The values of these parameters used in the calculations are summarized in Table I. Here we consider only zinc-blende CdS and ZnTe.

Having obtained the eigenstates in the conduction and valence bands, we can calculate the binding energy  $E_b$  of an electron-hole pair due to the Coulomb interaction,

$$E_b = \int d\mathbf{r}_1 \int d\mathbf{r}_2 \frac{|\psi_e(\mathbf{r}_1)|^2 |\psi_h(\mathbf{r}_2)|^2}{\bar{\epsilon}_0 |\mathbf{r}_1 - \mathbf{r}_2|}, \tag{7}$$

where  $\psi_e$  and  $\psi_h$  are the eigen functions of a conduction electron and a valence electron, respectively, and  $\bar{\epsilon}_0$  is the dielectric constant of the system, which is approximated in the calculations to be the simple average of the dielectric constants for the core and the shell materials,  $\bar{\epsilon}_0 = (\epsilon_0^{\text{core}} + \epsilon_0^{\text{shell}})/2$ .

#### IV. RESULTS AND DISCUSSIONS

In this section, we discuss in detail the electronic structures and wave functions as well as their dependence on the dimensions of InP-CdS and InP-ZnTe nano rods. To simplify

TABLE I: Material parameters used in the calculations [17–23].

Parameter	InP	CdS	ZnTe
$m_c$	$0.0790m_0$	$0.173m_0$	$0.16m_0$
$\gamma_1^L$	5.08	2.2	3.44
$\gamma_2^L$	1.60	0.35	0.59
$\gamma_3^L$	2.10	1.53	2.03
$E_g$ (eV)	1.42	2.56	2.39
$E_c$ (eV)	0.48	0.90	1.16
$E_v$ (eV)	-0.94	-1.60	-1.23
$\Delta$ (eV)	0.108	0.0	1.0
$a_c$ (eV)	-6.0	-3.59	-6.95
$a_v$ (eV)	-0.6	-1.51	-2.28
$b$ (eV)	-2.0	-0.5	-1.2
$d$ (eV)	-5.0	-3.7	-5.5
$e_{14}$	0.035	0.21	0.028
$C_{11}$ (GPa)	101.1	77.9	71.3
$C_{12}$ (GPa)	56.1	52.7	40.7
$C_{44}$ (GPa)	45.6	24.1	31.2
$a$	0.58697	0.582	0.610
$\epsilon_0$	12.5	8.5	10.4

our calculations while still capturing the essential physics, we consider coaxial, open-ended cylindrical core-shell nano rods, although in practice, the core at one end of the nano rod is capped by the shell material, as illustrated in Fig. 1. In the calculations, a cylindrical rod is arranged in such a way that its axis is along the  $z$ -axis, and the plane of  $z = 0$  is located at the half-height of the rod. The cylindrical coordinates  $(r, \theta, z)$  are used throughout the paper. We denote the core radius as  $R_1$ , the overall radius as  $R$ , and the height as  $H$ . The thickness of the shell is thus  $d \equiv R - R_1$ .

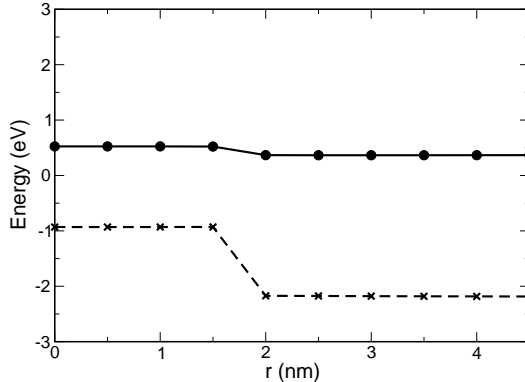


FIG. 2: Conduction (solid line) and valence (dashed line) band edges for a core-shell InP-CdS nano rod with  $H = 10$  nm,  $R = 5$  nm, and  $R_1 = 2$  nm. The circles and crosses represent the computational grid points at which the material is specified.

### A. Core-shell InP-CdS nano rods

First we show a typical band alignment of a core-shell InP-CdS nano rod. These band edges are obtained by minimizing the elastic energy due to strain and neglecting the kinetic energy of the electrons. Such band edges can be regarded as spatially dependent potentials for the valence and conduction electrons. We plot in Fig. 2 the conduction and valence band edges along the radial direction in the plane of  $z = 0$  for an InP-CdS nano rod with  $R = 5$  nm,  $H = 10$  nm, and  $R_1 = 2$  nm. It should be noted that the band alignment depends on the strain and therefore is a function of dimensions of the structure. We see from Fig. 2 that this nano rod exhibits a weak type-II band alignment, with the conduction band edge in the shell slightly lower than in the core. Thus in this structure, once an electron-hole pair is created in the core by photoexcitation, the electron (LUMO) tends to migrate to the shell while the hole (HOMO) remains in the core.

To demonstrate the spatial separation of electrons and holes, we define a radial charge distribution,  $D_1(r)$ , for an eigenstate,  $\psi$ ,

$$D_1(r) = \int dz \int d\theta r |\psi(r, \theta, z)|^2. \quad (8)$$

Figure 3 displays the radial charge distribution of the HOMO and LUMO. We see that the HOMO is predominantly distributed within the core ( $r < 2$  nm), whereas the LUMO is mainly localized in the shell ( $2 \text{ nm} < r < 5$  nm). These distributions clearly indicate the

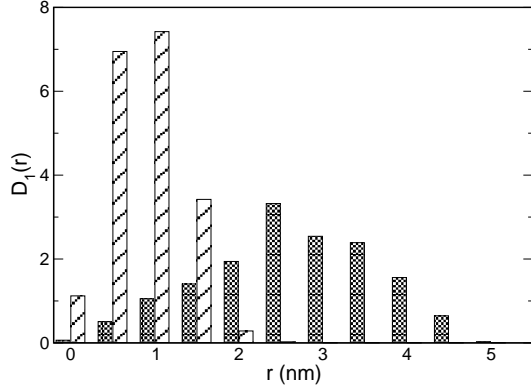


FIG. 3: Radial charge distribution  $D_1(r)$  of the HOMO (striped bars) and the LUMO (shaded bars) in the same structure as in Fig. 2.

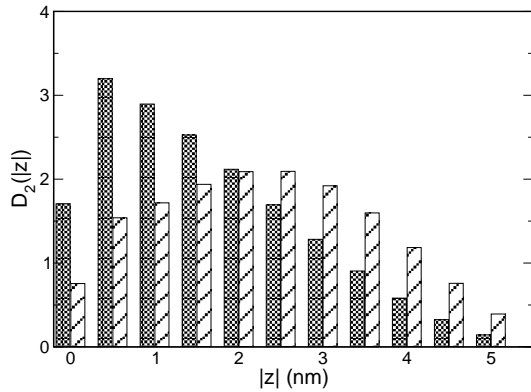


FIG. 4: Charge distributions of the HOMO (striped bars) and LUMO (shaded bars) along the  $z$ -axis in the same core-shell InP-CdS nano rod as in Fig. 2.

spatial separation of the HOMO and LUMO.

Moreover, the HOMO and LUMO also have different distributions along the  $z$ -axis. The distribution function along the  $z$ -axis is defined as

$$D_2(|z|) = 2 \int dr \int d\theta |\psi(r, \theta, z)|^2 \quad (9)$$

We see from Fig. 4 that the LUMO is mostly localized in the center of the nano rod ( $|z| < 2\text{nm}$ ), whereas the HOMO is localized outside the center ( $|z| > 2\text{nm}$ ). The different charge distributions of the HOMO and LUMO along the  $z$ -axis can be used to enhance their spatial separation to achieve faster charge transfer dynamics.

In a core-shell InP-CdS nano rod both the charge distributions and the energies of the

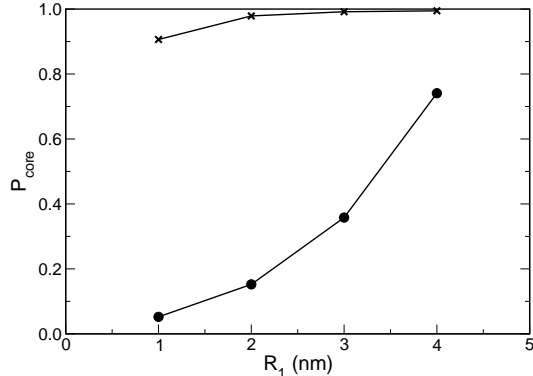


FIG. 5: Integrated charge distribution in the core  $P_{\text{core}}$  for the HOMO (crosses) and the LUMO (circles) as a function of  $R_1$  in core-shell InP-CdS nano rods with fixed  $R = 5$  nm and  $H = 2$  nm.

HOMO and LUMO can be tuned to a considerable degree by adjusting the dimensions of the structure. We define the integrated charge distribution in the core for an eigenstate as

$$P_{\text{core}} = \frac{\int_0^{R_1} dr D_1(r)}{\int_0^R dr D_1(r)}, \quad (10)$$

which measures whether an eigenstate is mainly in the core ( $P_{\text{core}} > 0.5$ ) or in the shell ( $P_{\text{core}} < 0.5$ ). Figure 5 shows  $P_{\text{core}}$  of the HOMO and LUMO as a function of core radius  $R_1$  in InP-CdS nano rods with fixed height  $H = 2$  nm and overall radius  $R = 5$  nm. We see that as the core radius increases and the shell thickness decreases (because of the fixed  $R$ ), the system undergoes a transition. At small core radii, the HOMO and the LUMO are well separated, with the HOMO predominantly in the core and the LUMO in the shell. With increase of the core radius, the LUMO gradually moves from the shell to the core, and eventually both the HOMO and the LUMO become localized in the core. This transition is understandable because as the core radius increases and the shell thickness decreases, the LUMO, initially localized in the shell, will feel a stronger quantum confinement, which in turn increases the electron kinetic energy. When the increased kinetic energy overcomes the conduction-band-edge offset between the core and the shell, the LUMO will have a lower energy in the core.

Spatial separation of photogenerated electrons and holes can greatly reduce their recombination (both radiative and nonradiative) probability. Although an accurate determination of the recombination rate requires a detailed computation of transition matrix elements, the recombination rate is approximately proportional to the square of wavefunction overlap

between the HOMO and the LUMO,  $\Phi^2$ , which can be estimated from the values of  $P_{\text{core}}$  of these states via

$$\Phi^2 \simeq P_{\text{core}}^H P_{\text{core}}^L + (1 - P_{\text{core}}^H)(1 - P_{\text{core}}^L), \quad (11)$$

where  $P_{\text{core}}^H$  and  $P_{\text{core}}^L$  are the  $P_{\text{core}}$  values for the HOMO and LUMO respectively. For the InP-CdS nano rods described in Fig. 5,  $\Phi^2$  changes from 0.74 at  $R_1 = 4$  nm, where both the HOMO and the LUMO are localized in the core, to 0.14 at  $R_1 = 1$  nm, where the HOMO and LUMO are spatially separated, indicating that the recombination lifetime can be significantly extended (5-fold) through the spatial separation of the HOMO and LUMO.

Apart from the charge distribution, the quantum confinement effects also change the energies of the HOMO and LUMO. We plot in Fig. 6 the HOMO energy ( $E_H$ ), the LUMO energy ( $E_L$ ), and the energy gap ( $E_g$ ) as a function of  $R_1$  in InP-CdS nano rods with fixed  $H = 2$  nm and  $R = 5$  nm. The gap in these heterostructures is actually the lowest exciton (electron-hole pair) energy, which can be calculated by

$$E_g = E_L - E_H - |E_b|, \quad (12)$$

where  $E_b$  is the binding energy resulting from the Coulomb interaction between the electron in the LUMO and the hole in the HOMO.  $E_g$  is the energy that will be used toward electrolyzing water and thus is an important property in hydrogen production. From Fig. 6, we see that as the core radius decreases from  $R_1 = 4$  nm to 1 nm, the HOMO energy changes from  $-1.08$  to  $-1.33$  eV, and the LUMO changes from  $0.72$  to  $0.56$  eV. Both energy changes are large enough to satisfy the overlap requirement in most situations [7], although for the HOMO the change is more pronounced. More important, these energy changes are in the *same* direction, meaning that both HOMO and LUMO can shift upward (downward) by increasing (reducing) the core radius to improve their overlap with  $\text{H}_2\text{O}$  redox potentials without significantly increasing the gap, which is an outstanding attribute of the InP-CdS nano rods as photoelectrodes.

The quantum confinement effects also manifest themselves when the height of an InP-CdS nano rod varies. We depict  $P_{\text{core}}$  for the HOMO and LUMO in Fig. 7 and the energies  $E_L$ ,  $E_H$ , and  $E_g$  in Fig. 8 as a function of  $H$  of InP-CdS nano rods with fixed  $R_1 = 2$  nm and  $R = 5$  nm. Figure 7 shows that as the height decreases the HOMO remains predominantly localized in the core, while the LUMO is concentrated in the shell and the charge density in the shell ( $1 - P_{\text{core}}$ ) is slightly enhanced. The smaller change of charge localization along

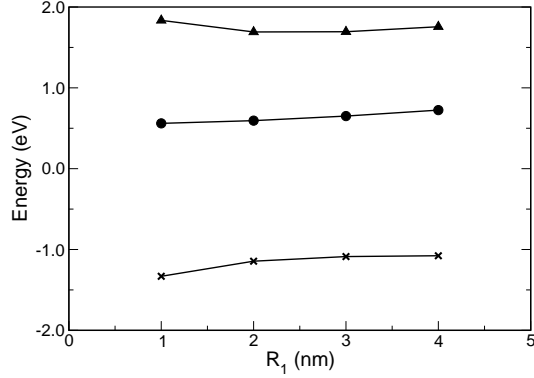


FIG. 6: Energies of the HOMO (crosses) and LUMO (circles) as well as the energy gap  $E_g$  (triangles) as a function of  $R_1$  in the same structure as in Fig. 5.

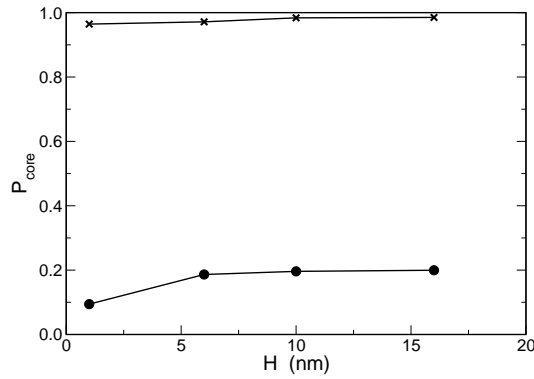


FIG. 7: Integrated charge distribution in the core  $P_{core}$  for the HOMO (crosses) and the LUMO (circles) as a function of  $H$  of core-shell InP-CdS nano rods with fixed  $R_1 = 2$  nm and  $R = 5$  nm.

the  $z$ -axis, as compared to that along the radial direction, is due to the enhancement or reduction of quantum confinement for both the core and the shell when the height varies. Figure 8 indicates that as the height of the nano rod decreases from  $H = 16$  nm to 1 nm, the HOMO energy changes from  $-1.04$  to  $-1.14$  eV, while the LUMO changes from  $0.45$  to  $0.87$  eV. Since the change in the LUMO energy is much more significant than that in the HOMO energy, one can adjust the height to improve the overlap with  $H_2O$  redox potentials in a situation where the conduction-band edge does not overlap with the  $H_2/H_2O$  potential but the valence-band edge does with the  $O_2/H_2O$  potential.

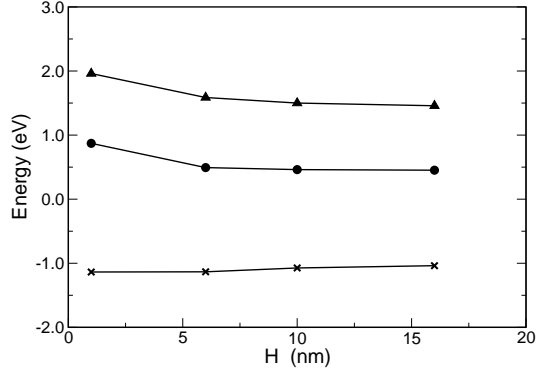


FIG. 8: Energies of the HOMO (crosses) and LUMO (circles) as well as the energy gap  $E_g$  (triangles) as a function of  $H$  in the same structure as in Fig. 7.

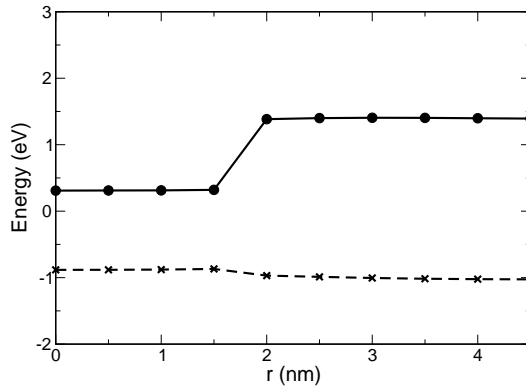


FIG. 9: Conduction (solid line) and valence (dashed line) band alignments for a core-shell InP-ZnTe nano rod with  $H = 10$  nm,  $R = 5$  nm, and  $R_1 = 2$  nm. The circles and crosses represent the computational grid points at which the material is specified.

## B. Core-shell InP-ZnTe nano rods

Figure 9 delineates conduction and valence band edges along the radial direction in the plane of  $z = 0$  for an InP-ZnTe nano rod with dimensions of  $R = 5$  nm,  $H = 10$  nm, and  $R_1 = 2$  nm. The band alignment of this InP-ZnTe nano rod is type-I, with similar valence band edges in the core and shell. Although the type-I band-alignment does not favor a spatial separation between electrons and holes, the small offset in the valence band edges can be overcome by adjusting the dimensions to realize the desired electron-hole separation for hydrogen production.

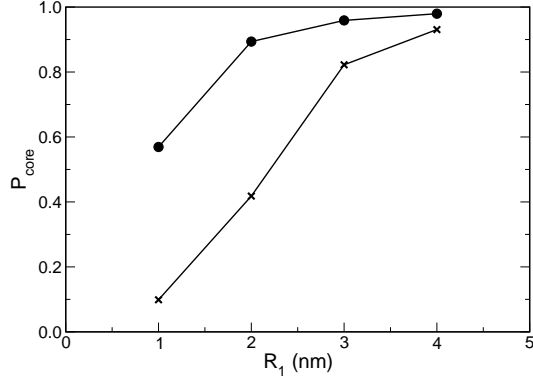


FIG. 10: Integrated charge distribution in the core  $P_{\text{core}}$  for the HOMO (crosses) and the LUMO (circles) as a function of  $R_1$  of core-shell InP-ZnTe nano rods with fixed  $H = 2$  nm and  $R = 5$  nm.

Figures 10 and 11 describe  $P_{\text{core}}$  and the energies  $E_H$ ,  $E_L$ , and  $E_g$  as a function of the core radius  $R_1$  in InP-ZnTe nano rods with fixed height  $H = 2$  nm and overall radius  $R = 5$  nm. We see from Fig. 10 a similar phase transition as in the InP-CdS nano rods (Fig. 3). For small core radii, strong quantum confinement squeezes the HOMO out of the core. Consequently, the HOMO and the LUMO are spatially separated with the LUMO in the core and the HOMO in the shell. For large core radii, however, the HOMO has a lower energy in the core and both the LUMO and the HOMO stay in the core. In the InP-ZnTe nano rods, charge distributions of both the HOMO and the LUMO strongly depends on  $R_1$ , which is in contrast with the situation in the InP-CdS nano rods described in Fig. 5, where the charge distribution of the HOMO depend weakly on  $R_1$ . This difference originates from the different band alignments illustrated in Figs. 3 and 9. Because of the spatial separation of the LUMO and HOMO at small radii,  $\Phi^2$ , the square of wavefunction overlap between the HOMO and the LUMO, decreases from 0.91 at  $R_1 = 4$  nm to 0.44 at  $R_1 = 1$ , suggesting the recombination lifetime becomes twice longer. According to Fig. 11, as the core radius decreases from  $R_1 = 4$  nm to 1 nm, the HOMO energy changes from  $-1.01$  to  $-1.05$  eV, while the LUMO energy changes from 0.80 to 1.28 eV. Thus in the InP-ZnTe nano rods, the LUMO energy can be shifted notably while the HOMO remains almost unchanged by adjusting the radial dimensions of the structures.

Interestingly, the phase transition of charge distribution also occurs as the height of the InP-ZnTe nano rods varies. Figure 12 shows how  $P_{\text{core}}$  depends on  $H$  of InP-ZnTe nano rods with fixed  $R_1 = 2$  nm and  $R = 5$  nm. According to Fig. 12, for a structure with the height

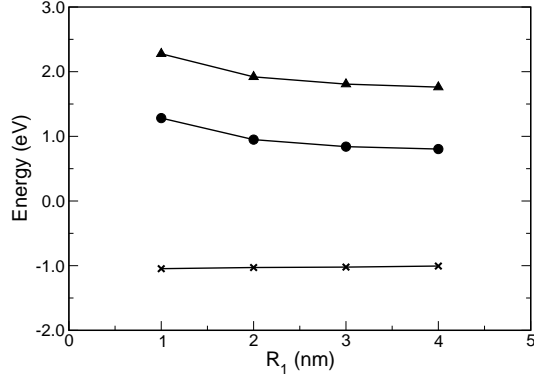


FIG. 11: Energies of the HOMO (crosses) and the LUMO (circles) as well as the energy gap  $E_g$  (triangles) as a function of  $R_1$  in the same structure as in Fig. 10.

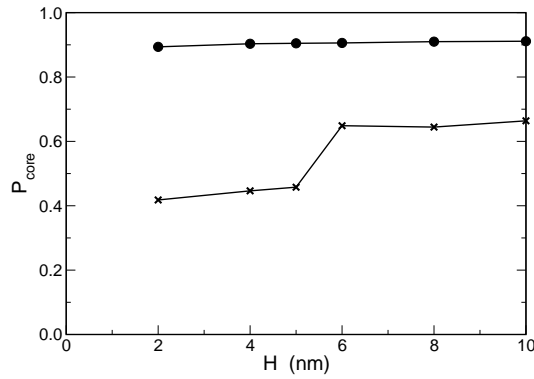


FIG. 12: Integrated charge distribution in the core  $P_{\text{core}}$  for the HOMO (crosses) and the LUMO (circles) as a function of the height of core-shell InP-ZnTe nano rods with fixed  $R_1 = 2$  nm and  $R = 5$  nm.

below 6 nm, the HOMO is mainly located in the shell, and the HOMO and LUMO are spatially separated, while for a structure with the height above 6 nm, the HOMO becomes localized in the core, and therefore the HOMO and LUMO stay in the same region. The dependence of the energies,  $E_H$ ,  $E_L$ , and  $E_g$ , on  $H$  in the same structures is illustrated in Fig. 13. Again, as the height decreases from 10 nm to 2 nm, the LUMO energy change, from 0.69 to 0.95 eV, is much more pronounced than the HOMO energy change, from  $-0.97$  to  $-1.03$  eV.

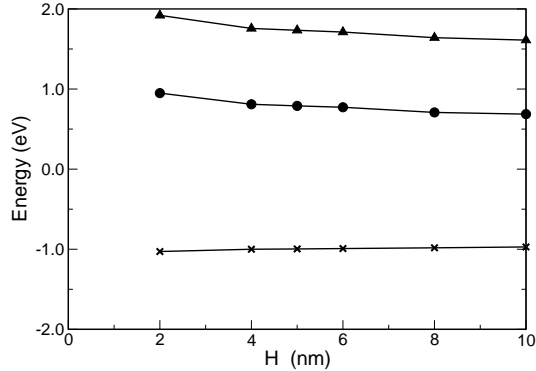


FIG. 13: Energies of the HOMO (crosses) and LUMO (circles) as well as the energy gap  $E_g$  (triangles) as a function of  $H$  in the same structures as in Fig. 12.

## V. CONCLUSIONS

We have systematically studied electronic structures and wave functions of core-shell nano rods using a strain-dependent  $k.p$  method. This study is aimed at identifying suitable semiconductor nanostructures as promising photoelectrodes for efficient PEC hydrogen production. We have shown that these core-shell nano rods exhibit a great tunability in terms of energies and wave-function distributions by varying the dimensions of the structures. This tunability enables us to design nanostructures with proper materials and dimensions to meet the criteria for an efficient photoelectrode.

We have examined these nano heterostructures against all the criteria and found that core-shell InP-CdS and InP-ZnTe nano rods are especially promising photoelectrodes for efficient PEC hydrogen production. In these nano rods, photoexcitation happens in the core whose band gap matches the solar spectrum to maximize the solar-to-hydrogen efficiency. These nano rods are stable in the aqueous environment because the smaller band gap core is protected by the larger band gap shell from corrosion in water. The HOMO and LUMO in these structures can be localized in different regions, diminishing the probability of electron-hole recombination. This separation also accelerates the charge transfer from the photoelectrode into water, and allows one to shift the HOMO and LUMO energies independently for achieving a desired overlap with the redox potentials in water.

InP-CdS and InP-ZnTe are especially good candidates for photoelectrodes because they have small discontinuities in the conduction and valence band edges respectively. This allows

one to effectively use quantum confinement and strain to achieve electron-hole separation and energy modification of the HOMO and LUMO. In the InP-CdS nano rods, electrons are localized in the shell and holes in the core, whereas in the InP-ZnTe structures, holes are localized in the shell and electrons in the core. Different electron-hole separation arrangements can be used in different aqueous conditions (e.g., different pH values) to achieve balanced electron and hole transfer rates, which is crucial for sustained hydrogen production.

### Acknowledgments

We are grateful to S. Krishnamurthy for helpful discussions. This work was supported by the Department of Energy under Contract DE-FC36-01GO11093.

- 
- [1] A. J. Bard and M. A. Fox, *Acc. Chem. Res.* **28**, 141 (1995).
  - [2] See, for example, A. Hagfeldt and M. Grätzel, *Chem. Rev.* **95**, 49 (1995).
  - [3] A. Bansal, O. Khaselev, and J. A. Turner, in *Proceedings of the 2000 DOE hydrogen program review*.
  - [4] K. Varner, S. Warren, and J. A. Turner, *Proceedings of the 2002 U.S. DOE Hydrogen Program Review NREL/CP-610-32405*.
  - [5] H. A. Finklea, *Semiconductor Electrodes* (Elsevier, Amsterdam, 1998).
  - [6] O. Khaselev, J. A. Turner, *J. Electrochem. Soc.* **316**, 57 (1991).
  - [7] S. S. Kocha, J. A. Turner, A. J. Nozik, *Electroanal. Chem.* **27**, 367 (1994).
  - [8] S. S. Kocha, J. A. Turner, *J. Electrochem. Soc.* **142**, 2625 (1995).
  - [9] N. Chandrasekharan and P. V. Kamat, *J. Phys. Chem.* **104**, 10851 (2000).
  - [10] H. Kato, K. Asakura, and A. Kudo, *J. Am. Chem. Soc.* **125**, 3082 (2003).
  - [11] L. P. Balet, S. A. Ivanov, A. Piryatinski, M. Achermann, and V. I. Klimov, *Nano Lett.* **4**, 1485 (2004).
  - [12] E. P. Pokatilov, V. A. Fonoberov, V. M. Fomin, and J. T. Devreese, *Phys. Rev. B* **64**, 245329 (2001).
  - [13] J. Li and L. W. Wang, *Appl. Phys. Lett.* **84**, 3648 (2004).
  - [14] C. Pryor, *Phys. Rev. B* **57**, 7190 (1998).

- [15] L. D. Landau and E. M. Lifshitz, *Theory of Elasticity* (Pergamon, London, 1959).
- [16] T. B. Bahder, Phys. Rev. B **41**, 11992 (1990).
- [17] I. Vurgaftman, J. R. Meyer, and L. R. Ram-Mohan, J. Appl. Phys. **89**, 5815 (2001).
- [18] A. B. Chen and A. Sher, *Semiconductor Alloys* (Plenum, New York, 1995).
- [19] P. Lawaeta, Phys. Rev. B **4**, 3460 (1971).
- [20] C. Hermann and C. Weisbuch, Phys. Rev. B **15**, 823 (1977).
- [21] D. Berlincourt, H. Jaffe, and L. R. Shiozawa, Phys. Rev. **129**, 1009 (1963).
- [22] A. Gavin and M. Cardona, Phys. Rev. B **1**, 672 (1970).
- [23] R. M. Martin, Phys. Rev. B. **6**, 4546 (1972).
- [24] D. W. Lucey, D. J. MacRae, M. Furis, Y. Sahoo, A. N. Cartwright, and P. N. Prasad, Chem. Materials, **17**, 3754 (2005), and references therein.
- [25] F. S. Manciu, R.E. Tallman, B.D. McCombe, B.A. Weinstein, D.W. Lucey, Y. Sahoo, and P.N. Prasad, Physica E **26**, 14 (2004).